International Journal of Multiphase Flow 197 (2026) 105624

Contents lists available at ScienceDirect

International Journal of Multiphase Flow

journal homepage: www.elsevier.com/locate/ijmulflow

Three-dimensional effects on carbon capture in wavy falling films☆

Andrea Düll [a,b], Alexander Nies [a], Álvaro Echeverría de Encio [a], Lyes Kahouadji [a], Seungwon Shin [c], Jalel Chergui [d], Damir Juric [d,e], Olaf Deutschmann [b], Omar K. Matar [a,*]

[a] Department of Chemical Engineering, Imperial College London, South Kensington Campus, London SW7 2AZ, United Kingdom
[b] Institute for Chemical Technology and Polymer Chemistry, Karlsruhe Institute of Technology (KIT), Engesserstraße 20, 76131 Karlsruhe, Germany
[c] Department of Mechanical and System Design Engineering, Hongik University, Seoul 04066, Republic of Korea
[d] Université Paris Saclay, Centre National de la Recherche Scientifique (CNRS), Laboratoire Interdisciplinaire des Sciences du Numérique (LISN), 91400 Orsay, France
[e] Department of Applied Mathematics and Theoretical Physics, University of Cambridge, Centre for Mathematical Sciences, Wilberforce Road, Cambridge CB3 0WA, United Kingdom

ARTICLE INFO

Keywords:
Falling film
Two-phase flow
CO_2 carbon capture
DNS

ABSTRACT

Wave evolution in thin-film flows is highly relevant for heat and mass transfer applications, such as CO_2 capture in falling film absorbers. To develop a detailed understanding of potential enhancement mechanisms associated with the evolution of three-dimensional (3D) waveforms, we perform 3D direct numerical simulations of passive scalar transport in laminar-wavy film flows, using a hybrid front-tracking/level-set method to accurately resolve interfacial features. CO_2 absorption is greatly enhanced in the presence of interfacial waves with the liquid-side mass transfer coefficient increasing tenfold relative to that of a flat film for the highest film Reynolds numbers (Re) studied. This is primarily due to changes in interfacial and internal flow dynamics rather than an increase in the gas-liquid interfacial area. The recirculation region present in the leading and trailing fronts of the 3D waves intensifies mass transfer, and their effectiveness increases with Re. At low Re, there is a film region beneath the wavy interface, which remains relatively undisturbed where mass transfer is dominated by diffusion. The introduction of structured substrates to promote mass transfer under these conditions is recommended. The visco-capillary ripple region, which precedes the leading and trailing fronts for sufficiently high Re, provides a relatively high degree of spanwise advection, with the mean spanwise velocity magnitude reaching around one-quarter that in the streamwise direction. This underscores the importance of solving the fully-3D problem as these effects do not have a two-dimensional analogue.

1. Introduction

Thin film flows are ubiquitous in nature, occurring on a wide range of length scales (Craster and Matar, 2009). On the kilometer-to-meter scale, they appear as geophysical phenomena such as gravity currents, mud flows, snow avalanches, and volcanic lava flows (Balmforth and Provenzale, 2011). At smaller scales — from millimeters to micrometers — they are observed in biological systems, including mucus flow in the pulmonary airways (Grotberg, 1994) and thin corneal tear films in the human eye (Craster and Matar, 2009). Industrially, thin film configurations are widely used in chemical engineering equipment such as reactors (Rößler et al., 2013), evaporators (Dai et al., 2022), crystallizers (Le Page Mostefa et al., 2015), and absorbers (Mortazavi et al., 2015), as well as on the surfaces of structured packing internals in absorption and distillation columns (Hampel et al., 2020).

Falling film flows also offer significant advantages for heat and mass transfer applications, including short contact time (critical for heat-sensitive fluids such as those in food processing), low pressure drop (advantageous for viscous liquids such as polymer solutions) and minimal holdup volume (essential when handling hazardous materials) (Al-husseini et al., 1998). The characteristic thin liquid layer and the large interfacial area of the falling film geometries promote exceptionally high specific heat and mass transfer rates (Charogiannis et al., 2015). These properties make them valuable in microfluidic systems, where surface-to-volume ratios can reach ~20 000 m^2/m^3 (Al-Rawashdeh et al., 2012).

The heat and mass transfer performance in falling film systems is closely tied to the underlying hydrodynamics. Issues such as liquid maldistribution and partial wetting can significantly impair transfer rates (Sebastia-Saez et al., 2013). In contrast, the development of interfacial waves can markedly enhance liquid-side transport pro-

---

☆ This article is part of a Special issue entitled: 'Interfacial Multiphysics' published in International Journal of Multiphase Flow.

* Corresponding author.
E-mail address: o.matar@imperial.ac.uk (O.K. Matar).

https://doi.org/10.1016/j.ijmultiphaseflow.2026.105624
Received 18 May 2025; Received in revised form 22 October 2025; Accepted 17 January 2026

cesses (Park and Nosoko, 2003; Demekhin et al., 2007)—a factor especially important in mass transfer applications, where the diffusivity in the liquid phase is typically low (Park and Nosoko, 2003). Although such waves naturally emerge in falling films over extended flow distances (Brauner and Maron, 1982), various forcing strategies have been explored in the literature to deliberately increase film waviness and thus boost heat and mass transfer performance. These approaches include passive methods, such as incorporating structured surfaces (Davies and Warner, 1969; Düll et al., 2024), as well as active techniques, such as the use of acoustic wave excitation (Schröder, 2019).

In a groundbreaking experimental study of falling film flows along a vertical plane, Park and Nosoko (2003) successfully combined spatial and time-oscillatory perturbations to investigate their influence on interfacial wave dynamics. By placing a spanwise array of fine needles along the liquid distributor in contact with the film and vibrating the inlet tube, they studied the evolution of three-dimensional (3D) wave structures from two-dimensional (2D) wavefronts in a well-controlled manner. The evolving solitary waves are characterized by a teardrop-shaped hump with a series of capillary ripples at its front (Park and Nosoko, 2003). Vortex formation in this elevated hump leads to liquid renewal at the gas-liquid interface and significantly increases the mass transfer rates (Miyara, 2000; Nagasaki et al., 2002; Yoshimura et al., 1996).

At low Reynolds numbers $Re < 40$, the imposed spatial perturbations lead to rather weak spanwise modulations of the evolving two-dimensional wavefronts (Park and Nosoko, 2003). In contrast, at elevated Reynolds numbers $40 < Re < 100$, these wavefronts become highly unstable and turn into 3D horseshoe-shaped wave structures (Park and Nosoko, 2003). Although horseshoes retain the same teardrop-hump/capillary-ripple characteristic, the wavefront between them disintegrates into dimples (Park and Nosoko, 2003). The associated destruction of internal vortices was speculated to affect the characteristics of mass transfer and be responsible for the reduced wave-induced increase in the mass transfer coefficient at $Re > 40$ compared to $Re < 40$ (Park and Nosoko, 2003). At the same time, the capillary waves that precede the teardrop humps of adjacent horseshoes can interfere, resulting in the formation of complex chequer-board or herringbone patterns (Georg F. Dietze, 2011). Relatively strong spanwise liquid flow is induced in these areas, and associated mixing was hypothesized to be responsible for the significant enhancement of heat and mass transfer processes observed in 3D falling film flows (Georg F. Dietze, 2011; Dietze et al., 2014).

The above findings highlight the complex 3D dynamics of wavy falling film flows, emphasizing the need for accurate numerical modelling to unravel the evolving internal flow structures and to fully understand their impact on heat or mass transfer processes. However, most numerical simulations of falling film flows in heat and mass transfer applications were conducted on simplified 2D domains. These include studies of film flows on smooth (Albert et al., 2014; Chen et al., 2023; Zhang et al., 2022; Zhou and Prosperetti, 2020) and structured (Åkesjö et al., 2019; Chen et al., 2021; Dietze, 2018; Hidman et al., 2024; Lu et al., 2021; Ma et al., 2024) surfaces. Although some findings from 2D simulation frameworks may be transferable to the 3D domain Park and Nosoko (2003), potentially important spanwise flow patterns remain elusive. Moreover, complex 3D wave structures without a predominant direction can develop at higher Reynolds numbers, particularly in falling film flows on structured surfaces (Düll et al., 2025). A series of 3D volume-of-fluid simulations was conducted to study the wetting behaviour of falling film flows (Sebastia-Saez et al., 2013, 2015, 2017; Ataki and Bart, 2006; Iso and Chen, 2011; Wan et al., 2022), but these studies mostly focused on mesoscale phenomena under non-wavy flow conditions.

In a novel approach, Dietze et al. (2014) performed full-scale direct numerical simulations (DNS) of the Navier–Stokes equations to study the evolution of three-dimensional interfacial waves under the same flow conditions as those investigated experimentally by Park and Nosoko (2003) and Rohlfs et al. (2012). Their simulation results provide an accurate representation of the fine interfacial details observed experimentally (Park and Nosoko, 2003) and reveal a significant discrepancy between the flow dynamics in 2D and 3D. The evolving horseshoe waves result in a separation of the overall flow into an inertia-dominated region in the teardrop-shaped humps and a viscocapillary region (Dietze et al., 2014). Substantial spanwise recirculation patterns can be observed in both regions, and due to the absence of gravity in the spanwise direction, these patterns are highly complex flow features (Dietze et al., 2014). Batchvarov et al. (2020) used a similar approach to Dietze et al. (2014) to investigate the effect of insoluble surfactants on the wave dynamics of falling film flows. Likewise, Kahouadji et al. (2022) studied the natural transition from an initially smooth interface to a fully-3D falling film flow. However, to the best of our knowledge, the effect of 3D flow patterns on heat and mass transfer processes has not yet been investigated numerically.

In this study, we integrate an advection-diffusion equation of a passive scalar into the simulation framework used by Kahouadji et al. (2022). In this manner, we aim to extend the previously described DNS simulations of 3D wave dynamics in falling film flows, and complement earlier works on wave-induced heat or mass transfer enhancement performed on 2D numerical domains. We focus mainly on mass transfer processes and consider the absorption of carbon dioxide (CO_2) as our primary application case. Due to the relatively low mass diffusivity compared to, for example, thermal diffusivity, wave-induced internal convection is expected to have a particularly high potential for process intensification in such applications (Dietze, 2018). We anticipate that understanding wave-induced transport enhancement effects in well-defined wave structures, such as those investigated experimentally by Park and Nosoko (2003) and considered in our study, will help unravel the complex interaction between falling film hydrodynamics and species transport in naturally evolving 3D wavy film flows. Eventually, this knowledge may be applied to design optimized spatial and/or temporal flow perturbations to enhance the process and energy efficiency of gas-liquid contactors, such as falling film absorbers for CO_2 capture applications (Ghasem, 2023).

2. Problem formulation and numerical procedure

2.1. Governing equations

We consider the spatio-temporal evolution of a thin liquid film falling down an isothermal, rigid, and impermeable vertical plane in a three-dimensional (3D) domain as shown in Fig. 1. We model the film dynamics using a standard Cartesian coordinate system $\boldsymbol{x} = (x, y, z) \in [0, \lambda_x] \times [0, \lambda_y] \times [0, \lambda_z]$ where x, y, and z refer to the streamwise, spanwise, and wall-normal coordinates, and λ_x, λ_y, and λ_z denote the domain lengths in these directions, respectively. The liquid is assumed to be Newtonian and incompressible and the overlying gas acts as an infinite reservoir of CO_2 maintained at constant pressure ($p_\infty = 1$ atm) and temperature ($T_\infty = 294.15$K).

We use a single-fluid formulation to model the two-phase flow problem under consideration in which the continuity, momentum, and advection-diffusion equations are respectively expressed by:

$$\nabla \cdot \boldsymbol{u} = 0 \tag{1}$$

$$\rho \left(\frac{\partial \boldsymbol{u}}{\partial t} + \boldsymbol{u} \cdot \nabla \boldsymbol{u} \right) = -\nabla p + \nabla \cdot \mu \left(\nabla \boldsymbol{u} + \nabla \boldsymbol{u}^T \right) + \rho \boldsymbol{g} + \boldsymbol{F} \tag{2}$$

$$\frac{\partial C}{\partial t} + \boldsymbol{u} \cdot \nabla C = \mathcal{D}_l \nabla^2 C \tag{3}$$

where ρ and μ denote the local density and viscosity, t and $\boldsymbol{u} = (u, v, w)$ represent time and the fluid velocity vector wherein u, v, and w correspond to the streamwise, spanwise, and wall-normal velocity components, and C and p the solute concentration and fluid pressure,

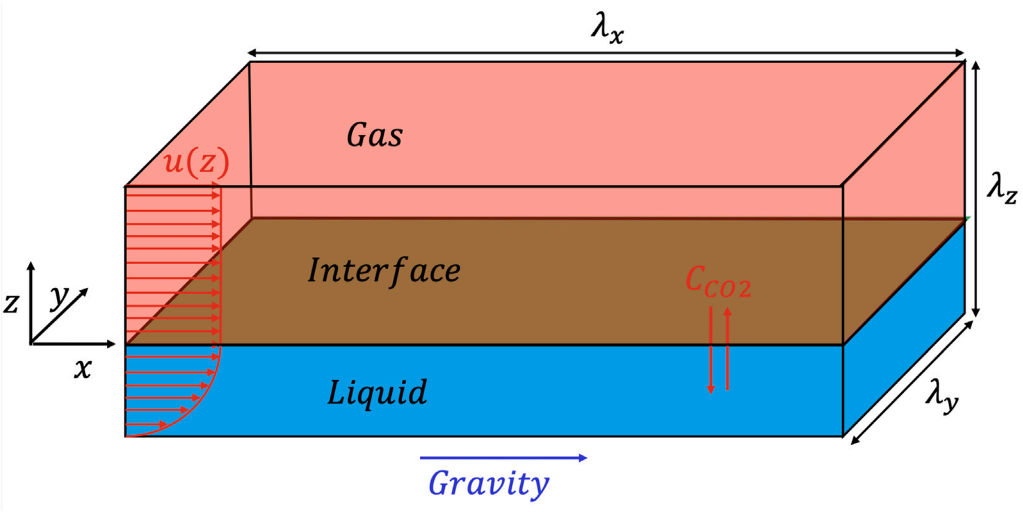

Fig. 1. Computational domain of a 3D falling film configuration with gas absorption.

respectively; $\boldsymbol{g} = (g, 0, 0)$ is the gravitational acceleration. Lastly, $\boldsymbol{F}$ is the local surface tension force at the interface modelled using a continuum surface force approach:

$$\boldsymbol{F} = \int_{A(t)} \sigma \kappa \hat{\boldsymbol{n}} \delta_D \left(\boldsymbol{x} - \boldsymbol{x}_f \right) dA \tag{4}$$

where $A(t)$ is the interfacial surface area, σ is the surface tension, κ the local curvature of the interface, and $\hat{\boldsymbol{n}}$ is the unit normal vector to the interface; $\delta_D \left(\boldsymbol{x} - \boldsymbol{x}_f \right)$ is a Dirac delta function in which $\boldsymbol{x}_f$ is the location of the interface.

Solutions of Eqs. (1) and (2) are obtained subject to no-slip and no-penetration conditions on the velocity and no-flux conditions on C at the solid substrate located at $z = 0$:

$$u = v = w = 0, \qquad \frac{\partial C}{\partial z} = 0 \tag{5}$$

Doubly-periodic conditions on $\boldsymbol{u}$ and p are imposed in the streamwise and spanwise directions. At $z = \lambda_z$, we impose free-slip and no-penetration conditions on the velocity and no-flux conditions on C, respectively:

$$\frac{\partial u}{\partial z} = v = w = 0, \qquad \frac{\partial C}{\partial z} = 0 \tag{6}$$

The initial concentration profile is defined in the entire domain using the Heaviside indicator function as $\mathcal{H}(\boldsymbol{x}, t)$:

$$C(\boldsymbol{x}, t = 0) = C_{g,0} + \left(C_{l,0} - C_{g,0} \right) \mathcal{H}(\boldsymbol{x}, t = 0) \tag{7}$$

The gas acts as an infinite source of solute with diffusion much faster than in the liquid, $\mathcal{D}_g \gg \mathcal{D}_l$. Thus, we ensure constant gas saturation with mass transfer limited by diffusion in the film:

$$C(\boldsymbol{x}, t) = C_{g,0} + \left(C_l - C_{g,0} \right) \mathcal{H}(\boldsymbol{x}, t) \tag{8}$$

The initial velocity of the falling film is described using the Nusselt theory, obtaining a parabolic velocity profile:

$$u_0(z) = \frac{\rho_l g \delta_0^2}{\mu_l} \left[\frac{z}{\delta_0} - \frac{1}{2} \left(\frac{z}{\delta_0} \right)^2 \right] \tag{9}$$

where δ_0 is the initial film thickness, and ρ_l and μ_l denote the liquid density and viscosity, respectively. The average velocity within the film is given by:

$$\bar{u}_0 = \frac{1}{\delta_0} \int_0^{\delta_0} u_0(z) dz = \frac{\rho_l g}{3\mu_l} {\delta_0}^2 \tag{10}$$

The initial spanwise and wall-normal component of the velocity are set to zero:

$$v(t = 0) = w(t = 0) = 0 \tag{11}$$

Table 1
Fluid properties for all the cases studied. Water (Park and Nosoko, 2003), DMSO (dimethylsulphoxide) and water mixture (Dietze et al., 2014), DMS-T12 (dimethylsiloxane) (Dietze et al., 2014).

Case	μ[Pa s]	ρ_l[kg/m^3]	σ[N/m]
1	8.9×10^{-4}	997.07	0.07201
2	3.1×10^{-3}	1098.3	0.0484
3	1.9×10^{-2}	949.0	0.020
Gas	1.8×10^{-5}	1.185	–

An initial disturbance is imposed on the film interface to drive wave formation:

$$\delta|_{t=0} = \bar{\delta} \left[1 + \epsilon_x \cos\left(k_x x \right) + \epsilon_y \cos\left(k_y y \right) \right] \tag{12}$$

where $\bar{\delta}$ is the average film thickness, $k_x = \frac{2\pi}{\lambda_x}$, $k_y = \frac{2\pi}{\lambda_y}$, $\epsilon_x = 0.2$ and $\epsilon_y = 0.05$ are taken as the same values as Dietze et al. (2014).

2.2. Scaling

To non-dimensionalize the governing equations, the following scalings are used:

$$\hat{\boldsymbol{x}} = \frac{\boldsymbol{x}}{\delta_0}, \quad \hat{\boldsymbol{u}} = \frac{\boldsymbol{u}}{\bar{u}_0}, \quad \hat{t} = \frac{t}{\delta_0 / \bar{u}_0}, \quad \hat{p} = \frac{p}{\rho_l \bar{u}_0{}^2}, \quad \hat{C} = \frac{C}{C_{sat}} \tag{13}$$

Using this scaling, the dimensionless forms of the governing equations are expressed as follows:

$$\nabla \cdot \hat{\boldsymbol{u}} = 0 \tag{14}$$

$$\frac{\partial \hat{\boldsymbol{u}}}{\partial t} + \hat{\boldsymbol{u}} \cdot \nabla \hat{\boldsymbol{u}} = -\nabla \hat{p} + \frac{1}{Re} \nabla^2 \hat{\boldsymbol{u}} + \frac{1}{Fr^2} \hat{\boldsymbol{k}} + \frac{1}{We} \int_{\hat{A}(\hat{t})} \hat{\sigma} \hat{\boldsymbol{\kappa}} \hat{\boldsymbol{n}} \delta_D \left(\hat{\boldsymbol{x}} - \hat{\boldsymbol{x}}_f \right) d\hat{A} \tag{15}$$

$$\frac{\partial \hat{C}}{\partial \hat{t}} + \hat{\boldsymbol{u}} \cdot \nabla \hat{C} = \frac{1}{Pe} \nabla^2 \hat{C} \tag{16}$$

where Re is the Reynolds number, which is the ratio of inertial to viscous forces, Fr is the Froude number, the ratio of inertial to gravitational forces, We is the Weber number, the ratio of inertial to capillary forces, and Pe is the (mass) Peclet number, which is the ratio of advective to diffusive transport:

$$Re = \frac{\rho_l u_0 \delta_0}{\mu_l}, \qquad Fr = \frac{u_0}{(g\delta_0)^{1/2}}, \tag{17}$$

$$We = \frac{\rho_l \delta_0 u_0^2}{\sigma}, \qquad Pe = \frac{u_0 \delta_0}{\mathcal{D}_l} = Re \cdot Sc \tag{18}$$

Table 2
Dimensionless numbers for all the cases studied.

Case	Re	Ka	We	Sc	Pe
1a	59.3	3923.0	6.3	510	30 090
1b				51	3009
2a	15.0	509.5	8.1	1610	24 190
2b				161	2419
3a	6.2	17.8	1.2	11 440	70 930
3b				1144	7093

Here, Sc represents the Schmidt number, which is the ratio of momentum to mass diffusivity:

$$Sc = \frac{\mu_l}{\rho_l \mathcal{D}_l} = \frac{Pe}{Re} \tag{19}$$

From the definition of Re, δ_0 can be expressed as a function of Re as follows:

$$\delta_0 = \left(\frac{3\mu_l^2}{\rho_l^2\, g} \right)^{\frac{1}{3}} Re^{\frac{1}{3}} \tag{20}$$

Other relevant dimensionless numbers are the Kapitza (Ka) and Sherwood (Sh) numbers. The former comprises physical parameters of the system rather than the characteristic velocity and length scales; the latter provides a dimensionless measure of the mass transfer rate:

$$Ka = \frac{\sigma}{\rho_l g^{1/3} \nu_l^{4/3}}, \qquad Sh = \frac{k_l}{\mathcal{D}_l/\delta_0} \tag{21}$$

where k_l corresponds to the overall mass transfer coefficient in the liquid phase.

The fluid physical properties of the three cases studied are summarized in Table 1. For each case, two simulations are performed: one with diffusion coefficient $\mathcal{D}_l = 1.75 \times 10^{-9}\ \mathrm{m^2/s}$ (Cases 'a') corresponding to the diffusivity of CO_2 in water at 294.15K (Versteeg and Van Swaaij, 1988), and the other with $\mathcal{D}_l = 1.75 \times 10^{-8}\ \mathrm{m^2/s}$ (Cases 'b'). The global dimensionless numbers for all the cases, except for Sh which will be calculated in Section 3, are shown in Table 2.

It should be noted that the aim is to explore the effect of hydrodynamics rather than that of different solvents on the absorption of CO_2. Hence, all cases used the same two diffusivity values mentioned above and the same saturation concentration of CO_2 at the interface $\left(C_{sat} = 37.8\ \mathrm{mol/m^3}\right)$.

2.3. Numerical procedure

Numerical solutions of the governing equations are obtained on a 3D Cartesian Eulerian grid using a hybrid level-set/front-tracking method (Batchvarov et al., 2020; Kahouadji et al., 2022; Shin et al., 2017, 2018). This approach employs a 2D triangular Lagrangian mesh to track the interface, which is immersed in the computational domain located at $\boldsymbol{x} = \boldsymbol{x}_f$. The numerical procedure uses a standard cell-centred scheme to compute spatial derivatives on the Eulerian grid except for convective terms for which a weighted essentially non-oscillatory (WENO) procedure on a staggered grid is utilized. The solutions are advanced in time using a second-order accurate Gear method; the viscous and diffusive terms are handled using an implicit time integration procedure.

To track the interface, a front-tracking method is used, and the interface is reconstructed via a level-set method approach; the Eulerian and Lagrangian grids are coupled using Peskin's immersed boundary method. Within the single-fluid formulation adopted, the density and viscosity are respectively given by

$$\rho = \rho_g \mathcal{H}\left(\boldsymbol{x} - \boldsymbol{x}_f\right) + \left(1 - \mathcal{H}\left(\boldsymbol{x} - \boldsymbol{x}_f\right)\right) \rho_l \tag{22}$$

$$\mu = \mu_g \mathcal{H}\left(\boldsymbol{x} - \boldsymbol{x}_f\right) + \left(1 - \mathcal{H}\left(\boldsymbol{x} - \boldsymbol{x}_f\right)\right) \mu_l \tag{23}$$

Table 3
Details of the computational domain and mesh discretization. The sub-domain mesh size is 32^3.

Case	Domain [cm^3]	Subdomains	Global Res.
1	$2.5 \times 2 \times 0.12$	$24 \times 18 \times 2$	$768 \times 576 \times 64$
2	$2.07 \times 2.07 \times 0.12$	$18 \times 18 \times 2$	$576 \times 576 \times 64$
3	$2.2 \times 3 \times 0.21$	$15 \times 18 \times 3$	$480 \times 576 \times 96$

where ρ_g and μ_g denote the density and viscosity of the gas phase, respectively; here, $\mathcal{H}(\boldsymbol{x} - \boldsymbol{x}_f)$ is a Heaviside indicator function computed directly from the interface, which vanishes everywhere except in the liquid phase but is smoothed over 3–4 grid points. The reconstructed interface is also used to generate $\hat{\boldsymbol{n}}$ and δ_d for the surface force $\boldsymbol{F}$ in Eq. (4).

The advection of the Lagrangian field according to $\boldsymbol{x}_f(t + \Delta t) = \int_t^{t+\Delta t} \boldsymbol{u}(\boldsymbol{x}_f, t) dt$, where $\boldsymbol{u}(\boldsymbol{x}_f, t)$ is the interpolated velocity at the interface at time t, is carried out using a second-order accurate Runge–Kutta method. The code used to carry out the computations based on this numerical procedure has been parallelized using an MPI protocol. The computational domain, the subdomain decomposition, and its global resolution for all cases are detailed in Table 3. The domain boundaries are used in the discussion section to non-dimensionalize the spatial variables for visualization.

3. Results and discussion

We present a discussion of the numerical results starting with the interfacial dynamics and mass transfer characteristics associated with various regions of the waves. We also trace the mechanisms underlying mass transfer enhancement and distinguish between the contributions to the wave-induced process intensification associated with the increase in interfacial area and the recirculation patterns that accompany the formation of large-amplitude interfacial waves.

3.1. Effect of bulk flow patterns on mass transfer

Fig. 2 provides a three-dimensional representation of the different interfacial structures obtained for the simulation Cases 1a-3a. The spatial distribution of the CO_2 concentration in the liquid phase is qualitatively represented by a colour map. Snapshots are shown at the time that liquid saturation reaches approximately 20%. The wavy structures are separated into three distinct regions: an inertia-dominated Region 'P' that encompasses the primary wave hump with a leading and a trailing front, Region 'C' corresponding to visco-capillary ripples, and Region 'F' represented by a quasi-flat, residual film. Due to the relatively low Re and We values associated with Case 3, no pronounced capillary ripples are observed.

We use a local Peclet number Pe' to assess the relative significance of advection to diffusion in the immediate vicinity of the interface:

$$Pe' = \frac{\|\boldsymbol{u}\|\delta}{\mathcal{D}_l} \tag{24}$$

where $\|\boldsymbol{u}\|$ is the local velocity magnitude and δ is the local film thickness. The spatial Pe' distributions are shown in Fig. 3 (left half-planes) for the same cases as in Fig. 2. The corresponding distributions of the normalized CO_2 concentration are also shown in the right half-planes of Fig. 3. The data were extracted directly below the gas-liquid interface, and the local concentration inhomogeneities are due to data sampling on the discrete numerical grid.

In all cases, the primary wave hump and, where present, the capillary ripples, exhibit high CO_2 concentrations indicating that these two regions are the main contributors to CO_2 absorption. On the one hand, high mass transfer rates and hence high local CO_2 concentrations are not surprising for the primary wave hump, as the elevated local Peclet

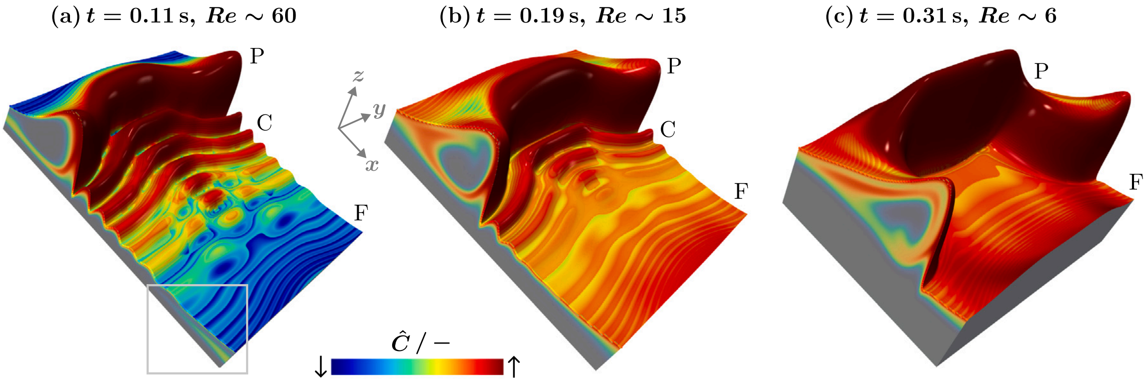

Fig. 2. DNS results for (a) Case 1a, (b) Case 2a, and (c) Case 3a. The colour map shows the spatial distribution of the normalized CO_2 concentration in the liquid film. The domains are clipped just beneath the gas-liquid interface and stretched in the z-direction for visibility. P: Primary wave hump, C: Capillary ripples, F: Residual film.

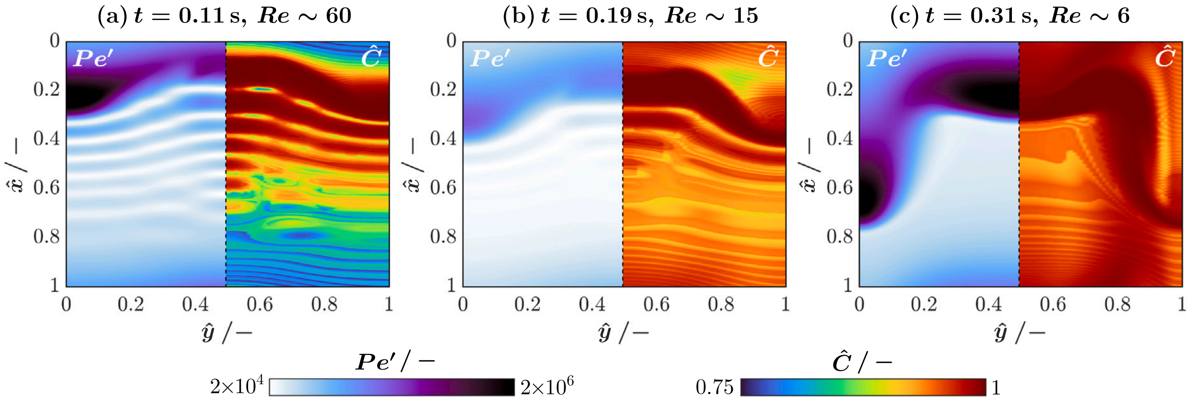

Fig. 3. Contours of the local Peclet number Pe' (left half-plane) and the normalized local CO_2 concentration $\hat{C} = C/C_{sat}$ (right half-plane) beneath the gas-liquid interface for (a) Case 1a, (b) Case 2a, and (c) Case 3a.

numbers suggest greater advection in this region compared to the other regions.

It is also interesting to see that the capillary ripple structures in Figs. 3a and b are just as saturated with CO_2 near the interface as the primary wave hump despite the much lower local Peclet numbers. This suggests that complex internal recirculation patterns are present even in flow regions with weaker interface distortion.

The residual film region also shows significant differences in the CO_2 concentration distribution near the interface between the three simulation cases. Figs. 2 and 3 illustrate that this region remains relatively lean in CO_2 for Case 3a (and Case 2a, to some extent). As highlighted by the rectangle in Fig. 2a, this is because the highly saturated liquid, extracted from the near-interface region by the recirculation zone in the primary wave hump, penetrates deeply into the bulk liquid film for Case 1a, while concentration redistribution remains confined to regions closer to the interface for the other two cases. This further contributes to the significant intensification of CO_2 absorption observed for Case 1a. The associated internal recirculation patterns are analysed in detail in the following.

The previously discussed differences in interfacial dynamics and CO_2 absorption characteristics are directly reflected in the internal flow patterns. Figs. 4aii-civ show the spatial distribution of absorbed CO_2 across the sampling slices in the (x, z) plane. As indicated in the 3D interface representations in Figs. 4ai-ci, the sampling planes are located in the centre of the numerical domain at $\hat{y} = 0.5$, after the first quarter of the domain at $\hat{y} = 0.25$, and at the outer periodic boundary of the domain at $\hat{y} = 0$. The corresponding concentration profiles CO_2 in the wall-normal direction z are shown in Fig. 5. They are extracted from the central sampling plane in the trailing front of the primary wave hump ('P'), the most pronounced capillary ripple ('C'), and the residual film region ('F'). In both figures, columns (a)–(c) are associated with Cases 1a-3a. Since the simulation Cases 1b-3b with increased diffusivity show identical flow behaviour and similar concentration profiles, their results are not included for the sake of brevity.

The streamlines, shown in Fig. 4 in a reference frame travelling with the waves, indicate that the large vortex previously reported for 2D waves (Park and Nosoko, 2003) is pronounced in the leading horseshoe-shaped front (see Fig. 4 aiv-civ) and in the trailing hump (see Fig. 4 aii–cii) of the 3D wave structures. The associated mixing zone is particularly extended in these steep wave fronts upstream of local flow reversal regions, where a large fraction of the liquid near the wave crest moves at streamwise velocities exceeding the average wave celerity, as shown in Fig. 6. As a result, elements of the highly saturated liquid are extracted from the near-interface region and transported to the more CO_2-lean internal film regions.

As shown in Fig. 5 (curve 'P'), this recirculation is quantitatively reflected by a strong deviation of the spatial CO_2 concentration distribution from the profile associated with the diffusion-controlled case, highlighting the dominance of advective transport throughout the wave hump. For Case 1a, Fig. 4aiv shows that the concentration redistribution in the leading horseshoe hump extends far into the underlying bulk liquid film. This affects not only the concentration field directly below the primary wave hump but also extends into the adjoining residual film, as can be seen from the non-monotonic concentration profile shown in Fig. 5a (curve F) associated with the otherwise diffusion-dominated flow region. This maintains steeper concentration gradients

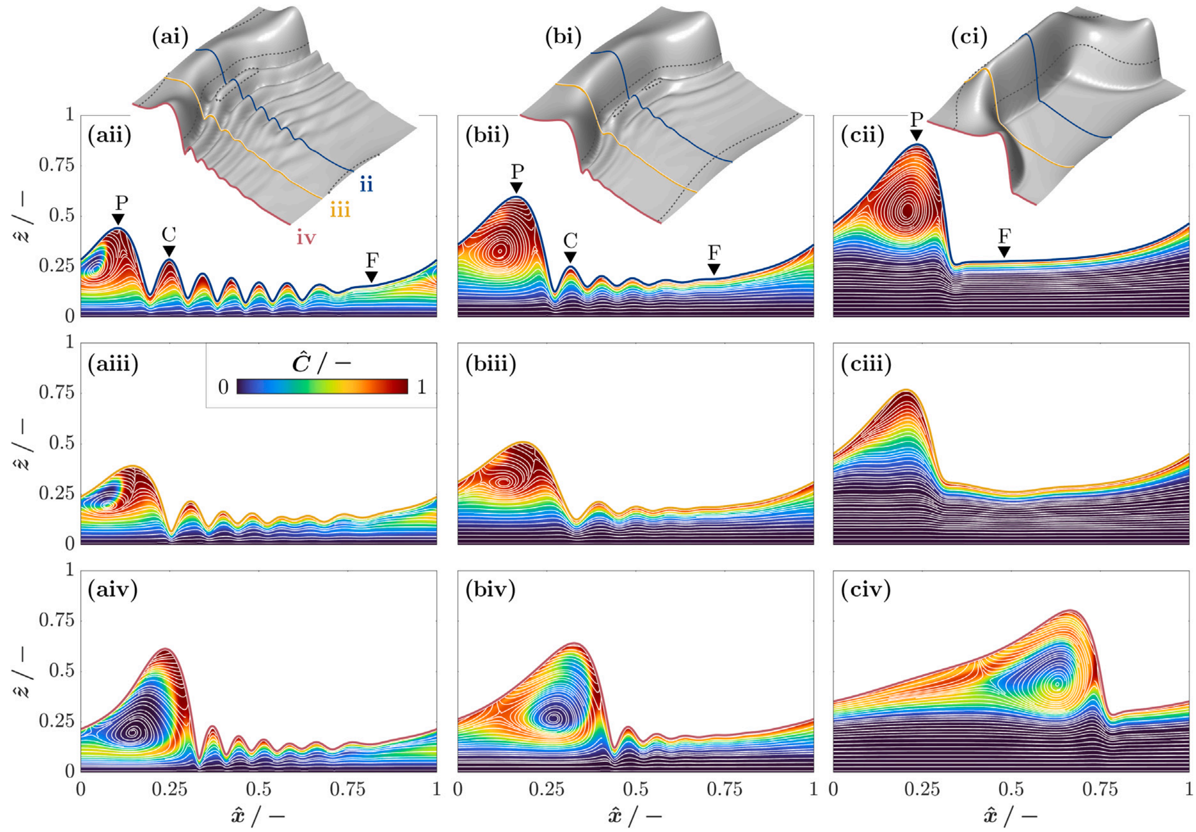

Fig. 4. Spatial distribution of the CO_2 concentration within the liquid film for (a) Case 1a at $t = 0.11$ s, (b) Case 2a at $t = 0.19$ s, and (c) Case 3a at $t = 0.31$ s. Subfigures (i) show the three-dimensional interface shapes, with the sampling locations in the xz-plane highlighted. Subfigures (ii)-(iv) show the concentration fields for the different slices, along with streamlines in the reference frame of the moving wave. The reference wave celerities u_w are (a) $0.43\,m/s$, (b) $0.33\,m/s$, and (c) $0.37\,m/s$.

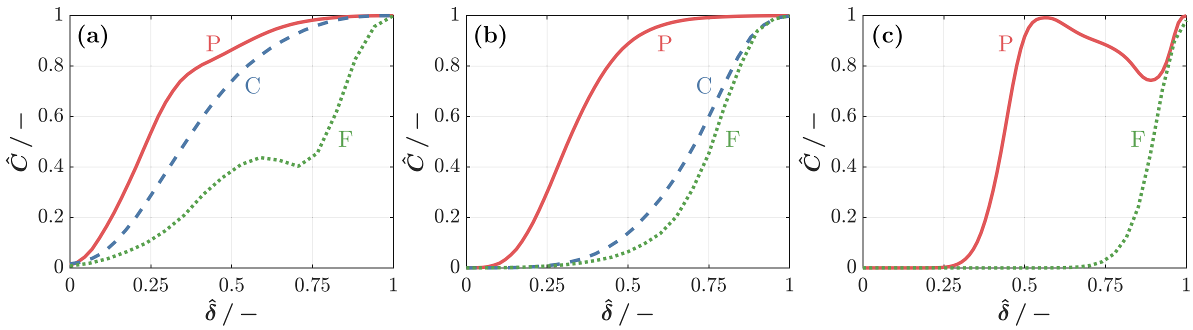

Fig. 5. Concentration profiles along the normalized film thickness $\hat{\delta}$ extracted centrally across the domain width in the primary wave (P), the capillary ripple (C) and the residual film region (F). The exact sampling locations are indicated in Figs. 4aii–cii. Columns (a)–(c) show the results for the simulation cases 1a–3a.

at the interface in the residual film regions compared to Cases 2a and 3a (see Fig. 4biv-civ), where the recirculation vortex is more spatially separated from the underlying bulk liquid phase and the highly saturated liquid accumulates at the upstream edge of the primary wave hump. Consequently, a larger fraction of the liquid phase participates in the absorption process for Case 1a, which is crucial for enhancing liquid-side mass transfer.

In contrast to the flow dynamics in the leading and trailing wave humps, the vortical structures in the intermediate connecting region are significantly weaker, as shown for simulation Cases 1a and 2a in Figs. 4aiii-biii; these structures disappear completely with increasing spatial separation between the two wave fronts, as shown for simulation Case 3a in Fig. 4ciii. As a result, local mass transfer rates decrease and, as can be observed from the figures, the CO_2 saturation front penetrates less deeply into the bulk liquid phase. However, pronounced spanwise mixing zones appear in the primary wave hump as the wave front takes on a distinctly 3D shape.

Fig. 7 shows representative examples for the three simulation cases in which the data were sampled in the (x, y) plane and the sampling location is indicated by dashed lines in Fig. 4ai-ci. As can be seen from the streamlines in the moving frame of reference, the spanwise recirculation patterns exhibit a wide variety of shapes. They can extend along the entire length of the wavefront (see Fig. 7a), but more localized mixing zones, such as those confined to the leading horseshoe hump, are also observed (see Fig. 7c). Although the spanwise liquid motion typically becomes more pronounced towards the crest of the primary wave, 3D internal flow patterns are still observed relatively close to the wave trough, as shown in Fig. 7b for simulation Case 2a. The close correspondence between the recirculation patterns and the CO_2 concentration fields underscores their significance to the absorption

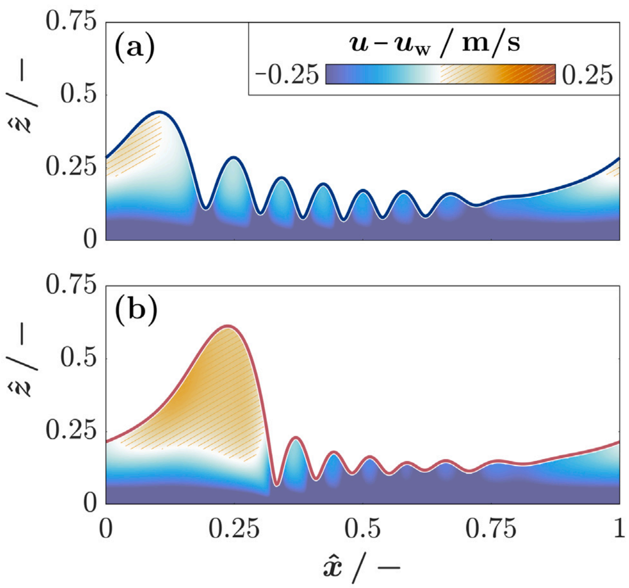

Fig. 6. Spatial distribution of the streamwise liquid velocity relative to the wave celerity of $u_w = 0.43\,\mathrm{m/s}$ for simulation Case 1a at $t = 0.11$ s. The sampling planes correspond to those in (a) Fig. 4aii and (b) Fig. 4aiv.

Table 4
Degree of spanwise advection R_{vu} in the trailing front of the primary wave hump (P_{trailing}), in the leading front of the primary wave hump (P_{leading}), in the capillary waves (C), and in the residual film region (F). Results are given for the three different simulation cases.

Region	Case 1	Case 2	Case 3
P_{trailing}	6.8%	4.1%	2.8%
P_{leading}	9.6%	9.5%	9.5%
C	10.4%	8.2%	–
F	0.6%	0.4%	0.2%

process. This observation has been facilitated by the 3D simulations carried out in this work.

The internal liquid motion in the spanwise direction is not limited to the primary wave hump, but it can also be observed beneath the capillary ripples preceding the elevated wave front. Table 4 quantifies the degree of spanwise advection $R_{vu} = \mathrm{mean}(v)/\mathrm{mean}(u)$ as the ratio between the mean absolute velocity in the spanwise direction (y) compared to that in the streamwise direction (x). The results for the different flow regions are determined from sampling slices in the (y, z) plane. Fig. 8 provides the corresponding qualitative recirculation patterns.

As can be gleaned from Table 4, the mean spanwise velocity magnitude in the capillary ripple region reaches approximately 10% of that in the streamwise direction. The values are significantly higher than those for the residual film region ($R_{vu} < 1\%$), where the film flow remains essentially 2D. Even in comparison to the primary wave hump, the degree of spanwise advection in the capillary ripple region exceeds that of its trailing front and falls within the same range as that of its highly distorted, horseshoe-shaped leading front. In particular, for Case 1a, the liquid velocity perpendicular to the main flow direction continues to increase as the capillary ripples take on a pronounced 3D shape with increasing residence time, reaching $R_{vu} \sim 24\%$ at $t = 0.22$ s.

The relatively high degree of spanwise advection compared to the more laminar simulation Case 2a may explain the discrepancy observed between the spatial CO_2 concentration profiles in Figs. 5a–b (curve 'C'). Although the concentration profile for Case 1a closely resembles that of the primary wave hump, the profile for Case 2a is more similar to that of the residual film region. These more pronounced convective mixing effects are another contributor to the higher mass transfer enhancement factors achieved in simulation Case 1a (Table 5). As shown in Fig. 9, they are associated with more pronounced flow reversal zones to higher interface curvatures.

In addition to the increasing degree of spanwise advection for Case 1a, the liquid transported in the crest of the capillary ripples can also accelerate with increasing residence time. Fig. 10 shows a representative example for a flow time of $t = 0.22$ s. The spatial distribution of the normalized concentration of CO_2 and the streamwise liquid velocity in the moving reference frame are given in Fig. 10(a) and (b), respectively. Once the liquid velocity in the crest of the highest capillary wave (indicated by the arrow) exceeds the wave celerity, a similar mass transfer enhancement effect can be observed as that previously described for the primary wave hump.

As evidenced by the highly distorted streamlines, complex flow patterns emerge and saturated liquid from the near-interface region is transported towards the wall region. Due to significant film thinning at the junction with the primary wave hump, the penetration depth of the concentration front is particularly high. This effectively counteracts the natural decrease in the wave-induced mass transfer enhancement (Dietze, 2018), which would otherwise have been observed when the liquid within the recirculation zone of the primary wave hump is fully saturated with CO_2. The latter is particularly detrimental for simulation Cases 3a and 3b, where the recirculation zone and the bulk liquid film are clearly spatially separated. As suggested in the literature based on 2D numerical simulations (Dietze, 2018), wall corrugations could be introduced in such cases to reactivate the intensification mechanism.

3.2. Effect of interfacial area on mass transfer

We examine the effect of the interfacial area resulting from wave formation on the enhancement of mass transfer. To estimate the liquid-side mass transfer coefficient k_l associated with the simulation results, we write down the following mass balance:

$$V_l \frac{d\overline{C}}{dt} = k_l A \left(C_{sat} - \overline{C} \right) \tag{25}$$

where A is the gas-liquid interfacial area and the liquid volume V_l within the domain remains is assumed to be constant. This equation captures the fact that the mass transfer results from the concentration difference between the saturated interface (C_{sat}) and the bulk liquid ($\overline{C}$). For CO_2 absorption into water at a temperature of 21°C and a pressure of 1atm, $C_{sat} = 37.8\ \mathrm{mol/m^3}$ (Dean and Lange, 1999; Sander, 2023). Integrating Eq. (25) for a constant $k_l A$ yields an expression for the instantaneous species concentration $\overline{C}$:

$$-\ln\left(1 - \frac{\overline{C}}{C_{sat}}\right) V_l = k_l A \cdot t \tag{26}$$

where we have assumed that the liquid phase is initially free of absorbed species, i.e. $\overline{C}(t = 0) = 0$. The overall volumetric mass transfer coefficient $k_l A$ can be obtained from a linear regression of Eq. (26) and division by the time-averaged gas-liquid interfacial area A obtained from the numerical simulations yields an estimate for the overall liquid-side mass transfer coefficient k_l, which can subsequently be used to calculate the overall Sherwood number Sh according to Eq. (21). Fig. 11 shows a representative regression plot for Case 2a.

To assess the intensification of the liquid-side mass transfer as a result of wave formation, a reference case in which no interfacial waves develop is required. In this study, Higbie's penetration theory (Higbie, 1935) is used to estimate the mass transfer coefficients for flat falling film flow. The key assumptions of penetration theory are that the gas and liquid phases are in equilibrium, unsteady mass transfer by diffusion occurs in the liquid elements residing at the interface, each liquid element remains in contact with the gas phase for the same duration before moving back from the interface to the fully-mixed bulk liquid, and the species penetration depth is small compared to the film thickness (Kraume, 2020). The corresponding liquid-side mass

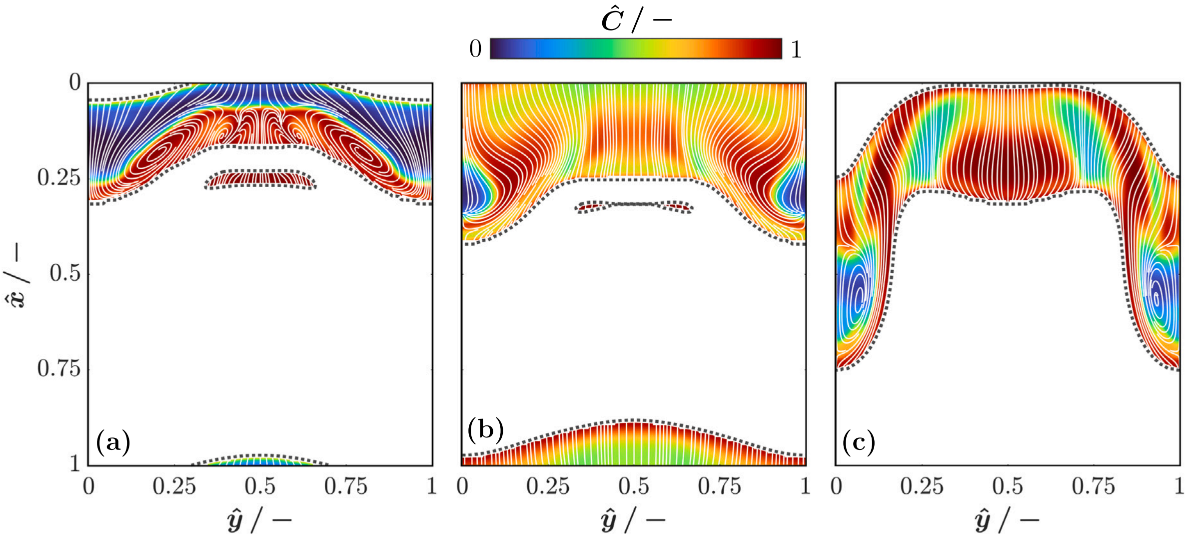

Fig. 7. Spatial distribution of the CO_2 concentration within the liquid film for (a) Case 1a at $t = 0.11$ s, (b) Case 2a at $t = 0.19$ s, and (c) Case 3a at $t = 0.31$ s. Results are shown for sampling planes in the xy-direction, indicated by dashed lines in Figs. 4ai–ci. The streamlines are determined for the reference frame of the moving wave, with the same reference wave celerities as in Fig. 4.

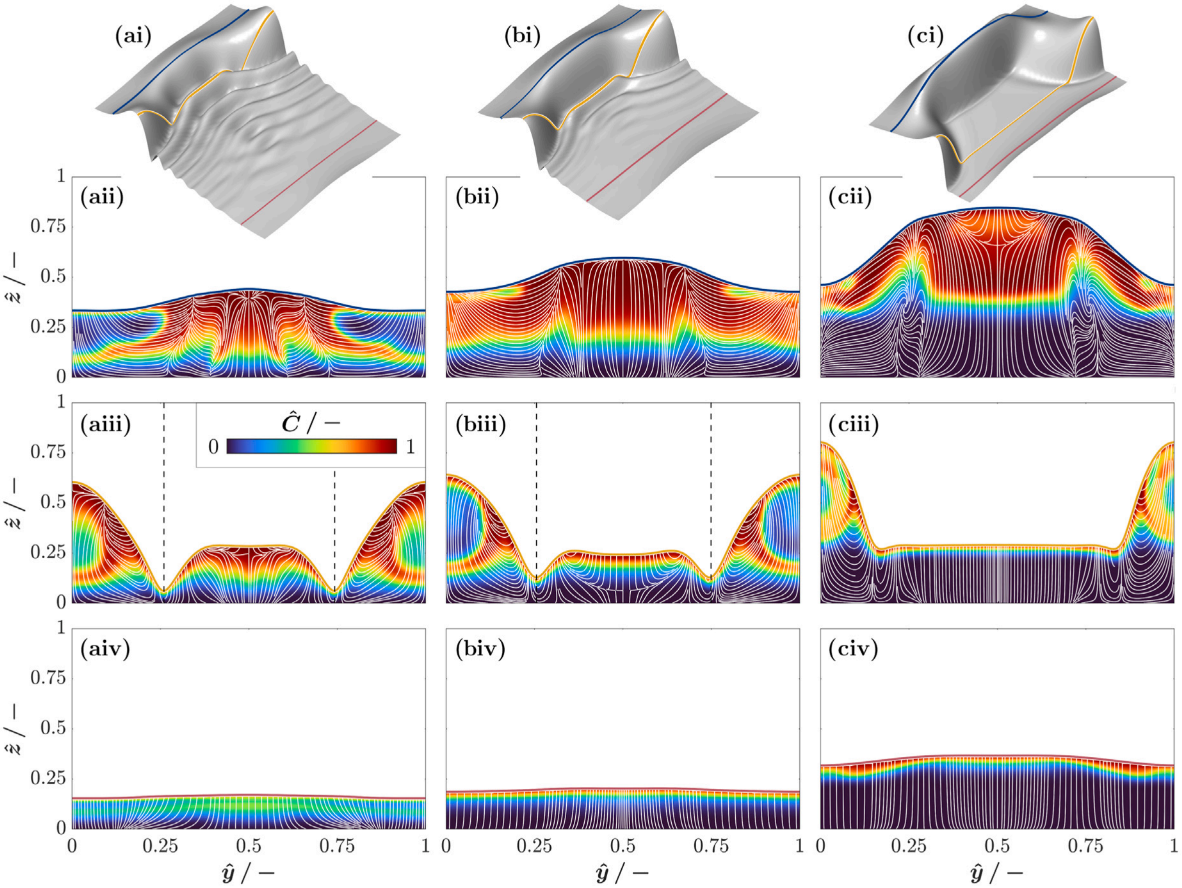

Fig. 8. Spatial distribution of the CO_2 concentration within the liquid film for (a) Case 1a at $t = 0.11$ s, (b) Case 2a at $t = 0.19$ s, and (c) Case 3a at $t = 0.31$ s. Subfigures (i) show the three-dimensional interface shapes, with the yz-sampling planes highlighted. The remaining subfigures show the concentration fields for (ii) the trailing primary wave hump, (iii) the leading primary wave hump, and (iv) the residual film region. For Case 1a and 2a, the capillary ripple region is marked in (aiii) and (biii) by dashed vertical lines. Streamlines are shown in the wall-fixed reference frame.

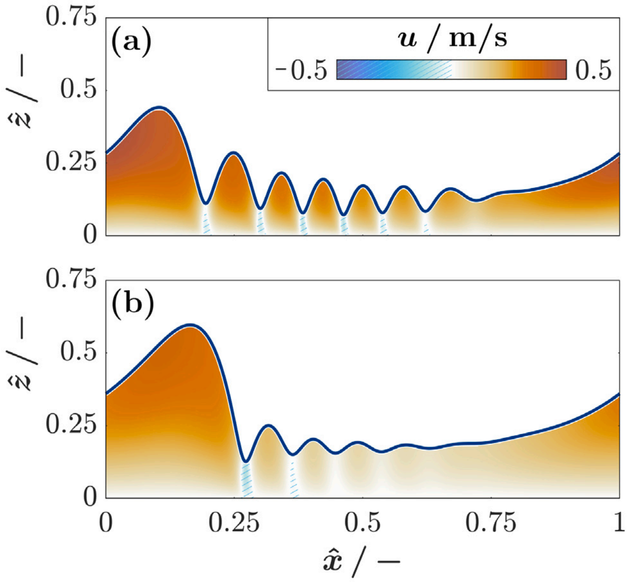

Fig. 9. Spatial distribution of the streamwise liquid velocity corresponding to (a) simulation Case 1a in Fig. 4aii and (b) simulation Case 2a in Fig. 4bii. Local flow reversal zones are characterized by negative liquid velocities up to the gas-liquid interface.

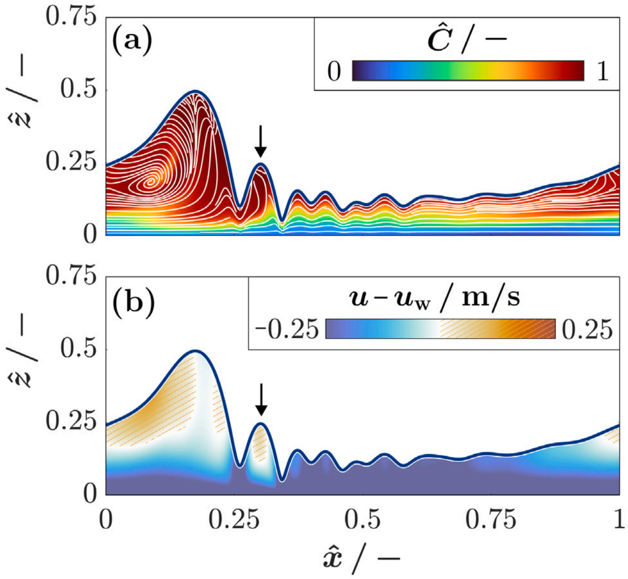

Fig. 10. Spatial distribution of (a) the normalized CO_2 concentration and (b) the streamwise liquid velocity relative to the wave celerity of $u_w = 0.43\,\mathrm{m/s}$ for simulation Case 1a at $t = 0.22\,\mathrm{s}$. Results are given for the central sampling slice in the xz-plane. As before, the streamlines in (a) are shown in the wave-fixed reference frame.

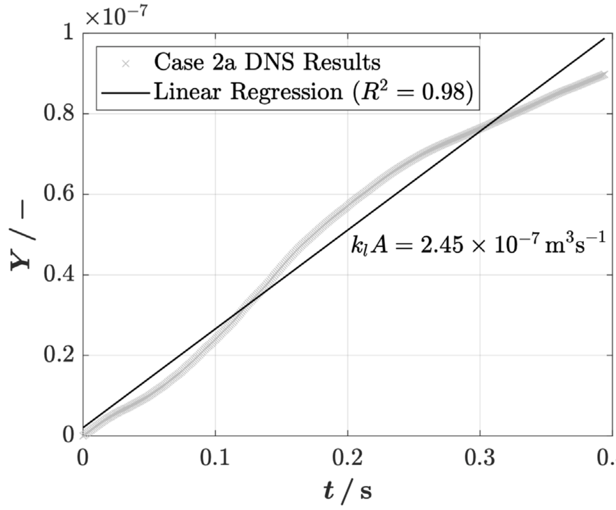

Fig. 11. Linear regression plot to estimate the volumetric mass transfer coefficient $k_l A$ for Case 2a. The variable Y plotted on the ordinate represents the left-hand side of Eq. (26).

Table 5
Reynolds number Re, liquid-side mass transfer coefficient k_l, mass transfer enhancement factor ε_k and Sherwood number Sh for each simulation case.

Case	Re	k_l [m/s]	ε_k	Sh
1a	59.3	8.68×10^{-4}	11.63	120.79
1b		9.26×10^{-4}	3.92	12.89
2a	15.0	5.70×10^{-4}	7.64	108.06
2b		6.52×10^{-4}	2.76	12.37
3a	6.2	6.49×10^{-4}	8.70	342.08
3b		7.50×10^{-4}	3.18	39.53

transfer coefficient $k_{l,\mathrm{P}}$, which is time-averaged over the complete contact period τ, is given by Eq. (27) (Kraume, 2020):

$$k_{l,\mathrm{P}} = 2\sqrt{\frac{D_l}{\pi\tau}} \tag{27}$$

The main quantitative data evaluation is conducted for simulation times of $t = 0\text{-}0.4\,\mathrm{s}$, i.e. $\tau = 0.4\,\mathrm{s}$. Finally, the wave-related mass transfer enhancement factor ε_k is defined as the ratio of the mass transfer coefficients obtained for wavy and flat films:

$$\varepsilon_k = \frac{k_l}{k_{l,\mathrm{P}}} \tag{28}$$

The calculated values of k_l and ε_k are summarized in Table 5. The wave-induced mass transfer enhancement is substantial in all cases, with a maximum mass transfer enhancement factor of $\varepsilon_k \sim 10$ achieved for Case 1a. The almost three-fold decrease in ε_k with a ten-fold increase in diffusivity between Cases 1a and 1b, the flow structures leading to mass transfer enhancement discussed above are less relevant for applications with high liquid-phase diffusivity, such as heat transfer.

Since the volumetric mass transfer coefficient $k_l A$ is directly proportional to the gas-liquid interfacial area A, the wave-induced area increase is of primary interest. Fig. 12 shows the corresponding area enhancement factor ε_A, which is calculated as the ratio of the interfacial area for each simulation case to that of a flat film. The determined area enhancement is of the order of $\sim 10^{-2}$, while the magnitude of the mass transfer enhancement factor ε_k in Table 5 is in the range of $\sim 10^0$. The significant discrepancy indicates that the wave-induced increase in interfacial area is of minor importance, even for the highly 3D wave shapes investigated in this study. Instead, other factors, such as wave dynamics at the gas-liquid interface and recirculation within the wavy film, are the most dominant contributors to enhancing mass transfer.

4. Conclusion

Three-dimensional (3D) direct numerical simulations of scalar transport in wavy falling liquid films were carried out for the first time. A hybrid front-tracking/level-set method was used to capture the deformation of the gas-liquid interface in detail. Due to its relevance in greenhouse gas reduction, the absorption of CO_2 was considered as the

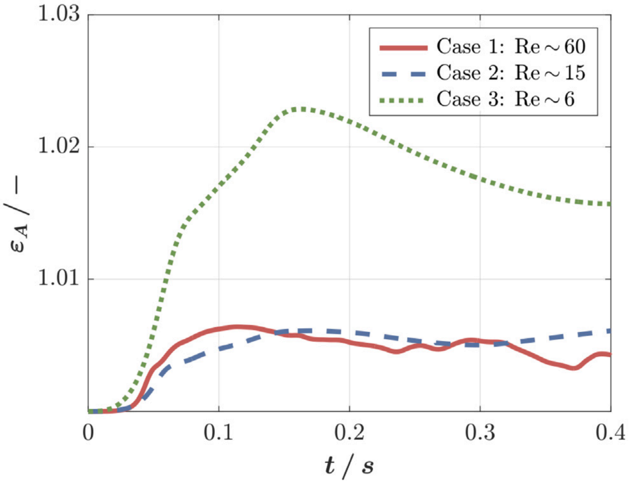

Fig. 12. Temporal evolution of the area enhancement factor ε_A for the three different simulation cases.

primary application case. The main objective was to develop a detailed understanding of the mass transfer enhancement mechanisms resulting from the evolution of three-dimensional wave structures.

Three different simulation cases with distinct spatio-temporal wave characteristics were analysed. Significant wave-induced mass transfer enhancement was found for all cases, with the liquid-side mass transfer coefficient increasing approximately tenfold relative to that of a flat liquid film for the highest Reynolds number studied. The increase in the interfacial area associated with the wave evolution is of minor importance, even for the highly 3D wave shapes investigated; changes in the interfacial and internal flow dynamics are much more influential in enhancing mass transfer.

The overall flow domain can be divided into an inertia-dominated primary wave hump, a capillary-dominated region of interfacial ripples, and a quasi-smooth residual film. The former two regions contribute to enhanced mass transfer under wavy flow conditions. For the primary wave hump, the large vortex in a reference frame moving with the wave, reported in the literature for two-dimensional waves, is present in both its trailing and leading front. It transports highly saturated liquid from near the interface towards the more CO_2-lean internal film regions. The recirculation zone is most extended in steep wave fronts upstream of local flow reversal zones, and the associated convective mixing effects are particularly pronounced when the concentration redistribution is not confined to the wave crest, but extends into the underlying bulk liquid film. This leads to higher concentration gradients near the gas–liquid interface and promotes the participation of a larger fraction of the liquid phase in the absorption process. As a result, the concentration field in the residual film region, which is otherwise almost purely diffusion-controlled, is also altered.

As the interfacial waves take on a more 3D shape, the recirculation vortex in the connecting region between the trailing and leading fronts of the primary wave diminishes. This adversely affects local mass transfer rates. At the same time, significant spanwise recirculation patterns evolve, which positively impact the absorption process. They are not limited to the primary wave, but are also present in the capillary ripple region. For the simulation case with the highest Reynolds number, the mean absolute liquid velocity in the spanwise direction reaches around 24% of that in the streamwise direction. Particularly strong enhancement effects are observed when the interfacial ripples accelerate with increasing residence time, and the internal flow behaviour becomes more similar to that of the primary wave.

The associated concentration redistribution, which leads to a particularly deep penetration of the saturation front into the liquid phase due to film thinning directly upstream of the ripple region, can counteract the natural decay in wave-induced mass transfer enhancement. The latter occurs when the liquid in the recirculation zone of the primary wave is fully saturated. This becomes particularly limiting for the most laminar simulation case studied, where the recirculation zone is spatially isolated from the underlying liquid phase. Structured surfaces can help to reactivate the mass transfer intensification mechanism under such flow conditions. As determined in a previous investigation (Düll et al., 2025), properly dimensioned two-dimensional surface structures can induce strongly oscillating 3D interfacial waves with highly beneficial effects on CO_2 absorption. The associated 3D mixing patterns will be analysed in future work using the same numerical simulation framework as that used in our present study.

CRediT authorship contribution statement

Andrea Düll: Writing – review & editing, Visualization, Validation, Methodology, Investigation, Formal analysis, Conceptualization. **Alexander Nies:** Writing – original draft, Visualization, Validation, Methodology, Investigation, Formal analysis. **Álvaro Echeverría de Encio:** Writing – original draft, Visualization, Validation, Methodology, Investigation, Formal analysis. **Lyes Kahouadji:** Writing – review & editing, Visualization, Validation, Methodology, Investigation, Formal analysis, Conceptualization. **Seungwon Shin:** Writing – review & editing, Software, Methodology. **Jalel Chergui:** Writing – review & editing, Software, Resources, Methodology. **Damir Juric:** Writing – review & editing, Software, Resources, Methodology. **Olaf Deutschmann:** Writing – review & editing. **Omar K. Matar:** Writing – review & editing, Supervision, Methodology, Investigation, Funding acquisition, Formal analysis, Conceptualization.

Declaration of competing interest

The authors declare the following financial interests/personal relationships which may be considered as potential competing interests: Omar Matar reports financial support was provided by Engineering and Physical Sciences Research Council. Andrea Dull reports financial support was provided by Friedrich and Elisabeth Boysen Foundation. If there are other authors, they declare that they have no known competing financial interests or personal relationships that could have appeared to influence the work reported in this paper.

Acknowledgements

This work is supported by the Engineering and Physical Sciences Research Council, United Kingdom, United Kingdom, through the EPSRC Programme Grants, MEMPHIS (EP/K003976/1) and PREMIERE (EP/T000414/1). O.K.M. acknowledges the Royal Academy of Engineering for a Research Chair in Multiphase Fluid Dynamics. We also acknowledge the HPC facilities provided by the Research Computing Service (RCS) of Imperial College London. D.J. and J.C. acknowledge support through computing time at the Institut du Developpement et des Ressources en Informatique Scientifique (IDRIS) of the Centre National de la Recherche Scientifique (CNRS), coordinated by Grand Equipement National de Calcul Intensif (GENCI) Grant 2025 A0182B06721. A.D. gratefully acknowledges financial support by the Friedrich and Elisabeth Boysen Foundation (Project-ID Boy-165) and the Karlsruhe House of Young Scientists (KHYS). Simulations have been performed using code BLUE (Shin et al., 2017).

Data availability

Data will be made available on request.

References

Åkesjö, A., Gourdon, M., Vamling, L., Innings, F., Sasic, S., 2019. Modified surfaces to enhance vertical falling film heat transfer – an experimental and numerical study. Int. J. Heat Mass Transfer 131, 237–251.

Al-Rawashdeh, M., Cantu-Perez, A., Ziegenbalg, D., Löb, P., Gavriilidis, A., Hessel, V., Schönfeld, F., 2012. Microstructure-based intensification of a falling film microreactor through optimal film setting with realistic profiles and in-channel induced mixing. Chem. Eng. J. 179, 318–329.

Albert, C., Marschall, H., Bothe, D., 2014. Direct numerical simulation of interfacial mass transfer into falling films. Int. J. Heat Mass Transfer 69, 343–357.

Alhusseini, A.A., Tuzla, K., Chen, J.C., 1998. Falling film evaporation of single component liquids. Int. J. Heat Mass Transfer 41 (12), 1623–1632.

Ataki, A., Bart, H.-J., 2006. Experimental and cfd simulation study for the wetting of a structured packing element with liquids. Chem. Eng. Technol. 29 (3), 336–347.

Balmforth, N.J., Provenzale, A., 2011. Geomorphological Fluid Mechanics. Springer.

Batchvarov, A., Kahouadji, L., Constante-Amores, C.R., Gabriel Farah Norões Gonçalves, S.S., Chergui, J., Juric, D., Craster, R.V., Matar, O.K., 2020. Three-dimensional dynamics of falling films in the presence of insoluble surfactants. J. Fluid Mech. 906 (11).

Brauner, N., Maron, D.M., 1982. Characteristics of inclined thin films, waviness and the associated mass transfer. Int. J. Heat Mass Transfer 25 (1), 99–110.

Charogiannis, A., An, J.S., Markides, C.N., 2015. A simultaneous planar laser-induced fluorescence, particle image velocimetry and particle tracking velocimetry technique for the investigation of thin liquid-film flows. Exp. Therm. Fluid Sci. 68, 516–536.

Chen, K., Liu, M., Gu, J., Mhamdi, A., Groß, S., Heng, Y., 2023. Efficient direct numerical simulation of gas absorption in falling films using a combined high-throughput/high-performance approach. Chem. Eng. Sci. 273, 118603.

Chen, S., Zhang, T., Lv, L., Chen, Y., Tang, S., 2021. Simulation of the hydrodynamics and mass transfer in a falling film wavy microchannel. Chin. J. Chem. Eng. 34, 97–105.

Craster, R.V., Matar, O.K., 2009. Dynamics and stability of thin liquid films. Rev. Modern Phys. 81 (08), 1131–1198.

Dai, Z., Zhang, Y., Wang, S., Nawaz, K., Jacobi, A., 2022. Falling-film heat exchangers used in desalination systems: A review. Int. J. Heat Mass Transfer 185, 122407.

Davies, J., Warner, K., 1969. The effect of large-scale roughness in promoting gas absorption. Chem. Eng. Sci. 24 (2), 231–240.

Dean, J.A., Lange, N.A., 1999. Lange's HandBook of Chemistry, fifteenth ed. McGraw-Hill, Inc..

Demekhin, E.A., Kalaidin, E.N., Kalliadasis, S., Vlaskin, S.Y., 2007. Three-dimensional localized coherent structures of surface turbulence. i. scenarios of two-dimensional–three-dimensional transition. Phys. Fluids 19 (11), 114103, 11.

Dietze, G.F., 2018. Effect of wall corrugations on scalar transfer to a wavy falling liquid film. J. Fluid Mech. 859 (11), 1098–1128.

Dietze, G.F., Rohlfs, W., Nährich, K., Kneer, R., Scheid, B., 2014. Three-dimensional flow structures in laminar falling liquid films. J. Fluid Mech. 743 (03), 75–123.

Düll, A., Lagadec, A.C.-L., Buchmüller, J., Häber, T., Ates, C., Börnhorst, M., 2024. Intensifying interfacial oscillations in falling film flows over rectangular corrugations. Phys. Fluids 36 (9), 09.

Düll, A., Lehmann, J., Börnhorst, M., Ateş, C., Häber, T., Deutschmann, O., 2025. Spatio-temporal characterization of the three-dimensional wave dynamics in falling film flows over rectangular corrugations. Exp. Fluids 66 (71).

Georg F. Dietze, R.K., 2011. Flow separation in falling liquid films. Front. Heat Mass Transf. 2 (3), 1–14.

Ghasem, N., 2023. Efficient co2 absorption through wet and falling film membrane contactors: insights from modeling and simulation. Sci. Rep. 13 (07).

Grotberg, J.B., 1994. Pulmonary flow and transport phenomena. Annu. Rev. Fluid Mech. 23 (1), 529–571, 01.

Hampel, U., Schubert, M., Döß, A., Sohr, J., Vishwakarma, V., Repke, J.-U., Gerke, S.J., Leuner, H., Rädle, M., Kapoustina, V., Schmitt, L., Grünewald, M., Brinkmann, J.H., Plate, D., Kenig, E.Y., Lutters, N., Bolenz, L., Buckmann, F., Toye, D., Arlt, W., Linder, T., Hoffmann, R., Klein, H., Rehfeldt, S., Winkler, T., Bart, H.-J., Wirz, D., Schulz, J., Scholl, S., Augustin, W., Jasch, K., Schlüter, F., Schwerdtfeger, N., Jahnke, S., Jupke, A., Kabatnik, C., Braeuer, A.S., D'Auria, M., Runowski, T., Casal, M.F., Becker, K., David, A.-L., Górak, A., Skiborowski, M., Groß, K., Qammar, H., 2020. Recent advances in experimental techniques for flow and mass transfer analyses in thermal separation systems. Chem. Ing. Tech. 92 (7), 926–948.

Hidman, N., Åkesjö, A., Gourdon, M., Jongsma, A., Ström, H., Sardina, G., Sasic, S., 2024. How surface modifications enhance vertical falling film evaporation. J. Fluid Mech. 997 (A17).

Higbie, R., 1935. The rate of absorption of a pure gas into a still liquid during short periods of exposure. Trans. Am. Inst. Chem. Eng. 31, 365–389.

Iso, Y., Chen, X., 2011. Flow Transition Behavior of the Wetting Flow Between the Film Flow and Rivulet Flow on an Inclined Wall. J. Fluids Eng. 133 (9), 091101, 09.

Kahouadji, L., Batchvarov, A., Adebayo, I.T., Jenkins, Z., Shin, S., Chergui, J., Juric, D., Matar, O.K., 2022. A numerical investigation of three-dimensional falling liquid films. Environ. Fluid Mech. 22 (03), 367–382.

Kraume, M., 2020. Transportvorgänge in der Verfahrenstechnik. Springer Vieweg Berlin, Heidelberg.

Le Page Mostefa, M., Muhr, H., Biget, A., Palasari, E., Fauconet, M., 2015. Intensification of falling film melt crystallization process through micro and milli-structured surfaces. Chem. Eng. Process.: Process. Intensif. 90, 16–23.

Lu, H., Lu, L., Gao, X., 2021. Mass transfer enhancement of falling film liquid desiccant dehumidification by micro-baffle plates. Int. J. Heat Mass Transfer 169 (04), 120945.

Ma, L., Ding, Y., Zhu, X., Wang, H., Liao, Q., 2024. Numerical investigation on falling film flow and heat transfer characteristics over corrugated plates. Int. J. Therm. Sci. 198 (01), 108 882–108 882.

Miyara, A., 2000. Numerical simulation of wavy liquid film flowing down on a vertical wall and an inclined wall. Int. J. Therm. Sci. 39 (9), 1015–1027.

Mortazavi, M., Nasr Isfahani, R., Bigham, S., Moghaddam, S., 2015. Absorption characteristics of falling film libr (lithium bromide) solution over a finned structure. Energy 87, 270–278.

Nagasaki, T., Akiyama, H., Nakagawa, H., 2002. Numerical analysis of flow and mass transfer in a falling liquid film with interfacial waves. Therm. Sci. Eng. 10 (1), 17–23, [Online]. Available: https://ndlsearch.ndl.go.jp/books/R000000004-I6059647.

Park, C.D., Nosoko, T., 2003. Three-dimensional wave dynamics on a falling film and associated mass transfer, vol. 49, (11), pp. 2715–2727, 11.

Rohlfs, W., Dietze, G.F., Haustein, H.D., Tsvelodub, Y.O., K.R, 2012. Experimental investigation into three-dimensional wavy liquid films under the influence of electrostatic forces. Exp. Fluids 53, 1045–1056.

Rößler, H., Wiesenhofer, W., Glasmacher-Remberg, C., Breucker, C., 2013. Thin-film reactors. In: Ullmann's encyclopedia of industrial chemistry. Wiley-VCH, Weinheim.

Sander, R., 2023. Compilation of henry's law constants (version 5.0.0) for water as solvent. Atmos. Chem. Phys. 23 (19), 10901–12440.

Schröder, T., 2019. Strömungscharakteristika und wärmeübertragung eines angeregten fallfilms.

Sebastia-Saez, D., Gu, S., Ranganathan, P., Papadikis, K., 2013. 3D modeling of hydrodynamics and physical mass transfer characteristics of liquid film flows in structured packing elements. Int. J. Greenh. Gas Control. 19, 492–502.

Sebastia-Saez, D., Gu, S., Ranganathan, P., Papadikis, K., 2015. Micro-scale cfd modeling of reactive mass transfer in falling liquid films within structured packing materials. Int. J. Greenh. Gas Control. 33, 40–50.

Sebastia-Saez, D., Reina, T.R., Arellano-Garcia, H., 2017. Numerical modelling of braiding and meandering instabilities in gravity-driven liquid rivulets. Chem. Ing. Tech. 89 (11), 1515–1522.

Shin, S., Chergui, J., Juric, D., 2017. A solver for massively parallel direct numerical simulation of three-dimensional multiphase flows. J. Mech. Sci. Technol. 31 (04), 1739–1751.

Shin, S., Chergui, J., Juric, D., Kahouadji, L., Matar, O.K., Craster, R.V., 2018. A hybrid interface tracking–level set technique for multiphase flow with soluble surfactant. J. Comput. Phys. 359, 409–435.

Versteeg, G.F., Van Swaaij, W.P.M., 1988. Solubility and diffusivity of acid gases (carbon dioxide, nitrous oxide) in aqueous alkanolamine solutions. J. Chem. Eng. Data 33 (01), 29–34.

Wan, Z., Wang, P., Shen, H., Li, Y., 2022. Falling film flow and heat transfer of cryogenic liquid oxygen on different structural surfaces. Energies 15 (14).

Yoshimura, P., Nosoko, T., Nagata, T., 1996. Enhancement of mass transfer into a falling laminar liquid film by two-dimensional surface waves—some experimental observations and modeling. Chem. Eng. Sci. 51 (8), 1231–1240.

Zhang, H., Gao, H., Gao, X., Yan, Y., 2022. Falling-film absorption model considering surface wave and vibration effects based on lattice boltzmann method. Energies 15 (21).

Zhou, G., Prosperetti, A., 2020. A numerical study of mass transfer from laminar liquid films. J. Fluid Mech. 902 (A10).